Journal of Materials Chemistry A

ROYAL SOCIETY OF CHEMISTRY

PAPER

View Article Online
View Journal | View Issue

Cite this: J. Mater. Chem. A, 2025, 13, 37604

Electrodeposition of N-heterocyclic carbene on mild steel surfaces

Vikram Singh, †[ac] Thilini M. Suduwella, †[ac] Anastasia Messina, [bc] Antoine Juneau, [ac] Mark D. Aloisio, [bc] Cathleen M. Crudden *[bc] and Janine Mauzeroll *[ac]

Received 18th July 2025
Accepted 24th September 2025

DOI: 10.1039/d5ta05828g

rsc.li/materials-a

N-heterocyclic carbenes (NHCs) are promising molecules for functionalizing and protecting metals, ranging from single crystals to polycrystalline samples. However, the functionalization of complex surfaces, such as mild steel (MS), a widely used industrial material, has only been scarcely explored, with only one prior report. Herein, we present a simple and highly reproducible electrochemical method to anchor NHCs onto MS surfaces. Two different NHC precursors are employed: ^{iPr}NHC·H_2CO_3 (1,3-diisopropylbenzimidazolium hydrogen carbonate) and ^{iPr}NHC^{Alk}·H_2CO_3 (1,3-diisopropyl-5-(prop-2-yn-1-yloxy)-1*H*-benzo[*d*]imidazol-3-ium hydrogen carbonate). Our electrochemical approach enables the controlled generation of nucleophiles at the interface between solvated NHCs and the MS surface. By tuning the electrochemical deposition parameters, we are able to optimize surface functionalization by regulating the generation of reactive oxygen species (ROS), and hydroxyl ions (OH^-). The resulting NHC coatings are characterized using microscopy, spectroscopy, and combined techniques such as AFM-IR. Stability tests reveal that these coatings are resistant to highly alkaline conditions.

Introduction

N-heterocyclic carbenes (NHCs) have recently garnered significant attention as superior alternatives to traditional thiol-based SAM precursors due to their enhanced binding affinity with metal surfaces.[1–4] Stable NHC thin films have been explored on a variety of pure metal surfaces, including Au[2,5–11] Pt,[6,12] Ag,[5] Cu[5,11,13] Ru,[14] Co[14] and Fe.[15,16] Deposition studies have also been extended to metal oxides (CuO_x,[11,14,17] FeO_x,[15] TiO_x[15]) both over single crystal and polycrystalline surfaces. Because of their high tunability, NHCs also provide versatile surface modification capabilities. By modifying NHC precursors with various functional groups, it becomes possible to create a variety of surface structures, ranging from self-limiting monolayers to thicker densely packed multilayer coatings. For instance, Berg *et al.*[13] demonstrated that NHCs modified with an alkyne group on the N-position (also referred as "wingtip") led to the formation of a 2 nm nanolayer on copper *via* acetylide-initiated polymerization. The proposed mechanism for NHC electrodeposition was said to proceed *via* direct electrochemical water reduction and generation of OH^-.[18] Hydroxide ion is then proposed to act as a base, deprotonating the imidazolium core (NR1–CH–NR1, pK_a = 22), or, in the case of alkyne-containing NHCs, the alkyne moiety as well (–O–CH_2–C≡CH, pK_a = 25).[13] Deprotonation of the alkyne group led to acetylide-initiated polymerization, and the formed multilayer was linked to the reduction of copper oxide, highlighting its potential for corrosion mitigation applications.[4,13]

Currently, most reports on the properties of NHC thin films focus on monometallic surfaces. However, a more complex yet widely used surface like mild steel (MS) is underexplored as a potential surface functionalization strategy with only one report in the literature.[19,20] MS is highly versatile and can be easily formed, welded, and machined, making it suitable for a wide range of applications across industries such as construction, automotive, manufacturing, and infrastructure.[21,22] Despite its widespread use, mild steel is particularly susceptible to corrosion.[23–27] Therefore, the prevention of corrosion on MS infrastructure is crucial to prevent failures, maintain structural integrity, and avoid costly repairs or replacements.[28] MS constitutes a complex surface due to its multi-metallic composition with variable surface segregation under variable exposure; these factors create a non-uniform and dynamic surface, making it a particularly challenging surface to functionalize.[3,25,29,30]

Herein, we explore the functionalization of MS surfaces using two benzimidazole-based NHC salts – one with a propargyl/alkyne (–OCH_2C≡CH) substitution on its aromatic ring and one without, namely ^{iPr}NHC^{Alk}·H_2CO_3 and ^{iPr}NHC·H_2CO_3

[a]Department of Chemistry, McGill University, Montréal, Québec, H3A 0B8, Canada. E-mail: janine.mauzeroll@mcgill.ca

[b]Department of Chemistry, Queen's University, Kingston, Ontario K7L 3N6, Canada. E-mail: cruddenc@chem.queensu.ca

[c]Carbon to Metal Coating Institute, Queen's University, Kingston, Ontario, K7L 3N6, Canada

† Equal contribution.

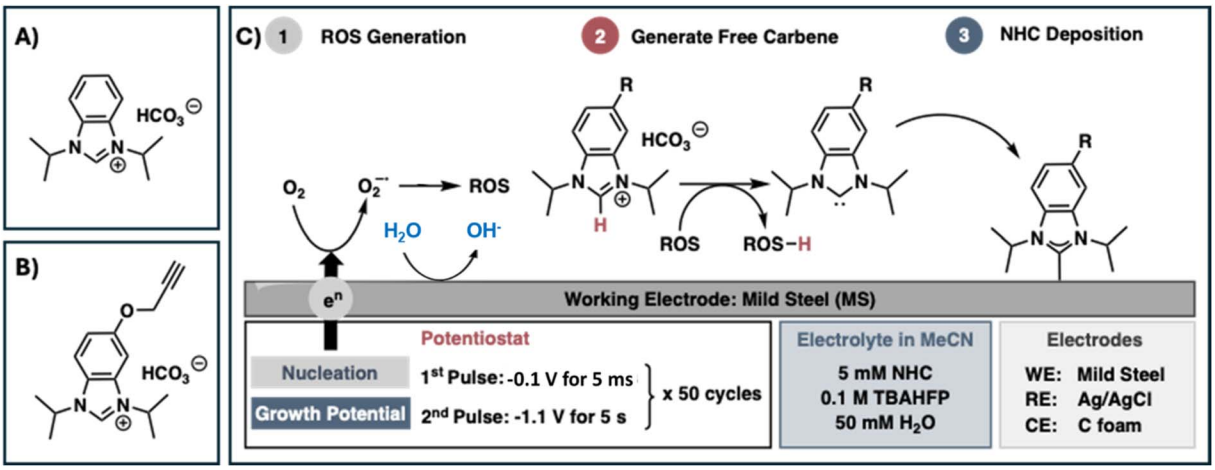

Scheme 1 NHC precursors used (A) 1,3-diisopropylbenzimidazolium hydrogen carbonate (^{iPr}NHC·H_2CO_3), and (B) 1,3-diisopropyl-5-(prop-2-yn-1-yloxy)-1*H*-benzo[*d*]imidazol-3-ium hydrogen carbonate (^{iPr}NHC^{Alk}·H_2CO_3). (C) Electrodeposition of NHC precursors on mild steel surfaces by precise control of the formation of free local carbene. Starting from the left, the first step is the "ROS and OH^- generation", where the *in situ* generation of these species is induced locally by applying a double pulse technique. During the first pulse, ROS species are generated, followed by OH^- formation in the second pulse. In step 2, "Free Carbene Generation" the resulting ROS and OH^- species from step 1, facilitate active proton abstraction from the NHCs precursors, leading to the formation of free carbenes. In step 3, "NHC deposition", the produced free carbenes in step 2 contribute to the formation of a NHC film on the MS surface. All measurements were conducted in MeCN electrolyte composed of 5 mM NHCs and 0.1 M NBu_4PF_6 in the presence of trace amount of water and inherently dissolved oxygen. R = –H, $-OCH_2C{\equiv}CH$.

(Scheme 1A and B), respectively. NHC deposition on steel was achieved through the deprotonation of imidazolium precursors by electrochemical generation of reactive oxygen species (ROS) and OH^- produced from inherently dissolved oxygen and intentionally added trace amounts of water, similar to reported literature for other substrates.[13,18]

Notably, while the role of water has previously been identified, we show that inherently dissolved O_2 plays a crucial role in the process and is required for the generation of ROS. With a thorough analysis employing various microscopic, spectroscopic, and combined measurement techniques, we investigated the expected formation of NHC thin layers on the MS surface. This study aims to assess the feasibility of forming NHC thin films on MS *via* electrodeposition, with the potential for further refinement for future applications toward primer film or surface passivation goals.

Results and discussion

The impact OF NHC chemistry on MS functionalization

The functionalization of MS *via* NHC electrochemical deposition was investigated with ^{iPr}NHC·H_2CO_3, due to its well-documented interaction with noble and non-noble metal surfaces.[2,11,31] A second precursor, ^{iPr}NHC^{Alk}·H_2CO_3, was selected due to the presence of an additional acidic proton on the alkyne moiety (Scheme 1), which we hypothesized could allow acetylide initiated polymerization, as reported by others for similar alkyne-containing structures.[13] Both compounds were synthesized *via* modifications to known procedures (see synthesis details in the SI).[20,32] These precursors were then deposited onto the MS surface by employing a double-pulse electrodeposition technique (Scheme 1C), which consists of two alternating negative potential applied for a specific number of cycles. We hypothesized that the use of two independent pulses could be beneficial to the polymerization, following a nucleation-growth process, and by altering the double layer.[33]

The success of the NHC electrodeposition on MS was first validated through scanning electron microscopy (SEM), confirming the presence of a deposited film, with different morphologies observed depending on the NHC employed (Fig. 1A–D). The use of ^{iPr}NHC-MS resulted in random island-like aggregates, whereas ^{iPr}NHC^{Alk}-MS exhibited more uniform, smaller and globular morphology aggregates. The uncoated MS sample (Ref-MS), included for comparison (Fig. 1A), and lacks such morphological features. To verify the nature of the aggregates, laser desorption/ionization-mass spectrometry (LDI-MS) was performed and the respective molecular ion species were observed at 203 *m*/*z* ($C_{13}H_{19}N_2^+$) for ^{iPr}NHC-MS, and 257 *m*/*z* ($C_{16}H_{21}N_2O^+$) for ^{iPr}NHC^{Alk}-MS (Fig. 1E–G, S5 and S6 of the SI). As expected, no peak was observed for either of these species on the Ref-MS surface (Fig. 1G). The presence of trace supporting electrolyte $(C_4H_9)_4N^+$ was detected at 242 *m*/*z* for ^{iPr}NHC-MS, in contrast to the ^{iPr}NHC^{Alk}-MS, which appeared free of residual electrolyte.

AFM-IR analysis of NHC-functionalized MS

AFM-IR measurements on the NHC-coated MS were next employed to detect the presence of NHCs and assess their nanoscale distribution. Prior to AFM-IR measurements, the common characteristic stretching frequencies of both NHC precursors were predicted through density functional theory (DFT) simulations and confirmed through experimental FT-IR measurements (Fig. S7, SI). To assist with identifying NHC species in the coated samples, we analyzed their stretching

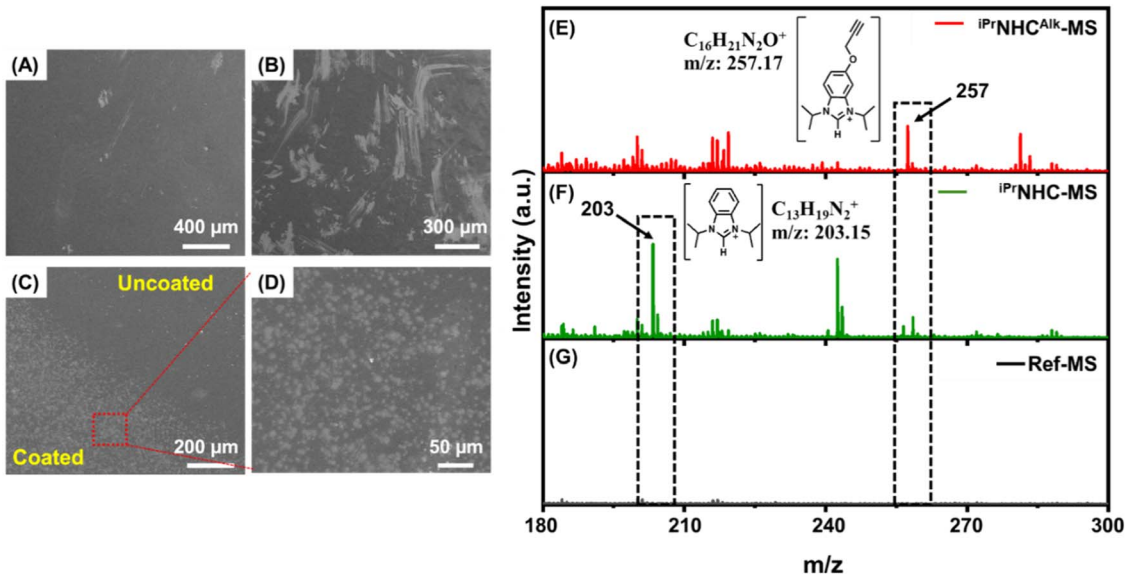

Fig. 1 Microscopic and spectroscopic evaluation of ^{iPr}NHC·H_2CO_3 and ^{iPr}NHC^{Alk}·H_2CO_3 functionalized MS surfaces. SEM images of the MS surface showing (A) Ref-MS (B) ^{iPr}NHC-MS (C and D) ^{iPr}NHC^{Alk}-MS at different magnifications. LDI-MS spectra exhibit pseudomolecular ion peaks at 257 *m/z* ($C_{16}H_{21}N_2O^+$) for (E) ^{iPr}NHC^{Alk}-MS and 203 *m/z* ($C_{13}H_{19}N_2^+$) for (F) ^{iPr}NHC-MS in comparison to the LDI-MS spectrum of unmodified MS (G) Ref-MS.

frequencies and correlated these with DFT-calculated spectra. Given that the operational IR frequency range in AFM-IR spans from 900 cm^{-1} to 1900 cm^{-1}, the characteristic vibrational frequencies of NHCs within this region were considered. Based on literature and DFT predicted IR spectra, the C–N stretching frequency of benzimidazolium ring appears at 1275 cm^{-1} (ref. 34–36) while the C–H wagging frequency in the propargyl group is observed at 1260 cm^{-1}.[37] Additionally, signals around 1680 cm^{-1} can be attributed to the C=O stretching frequency, which could be associated with urea derivatives of NHC produced during the deposition process in the NHC coated samples.[12,20]

AFM images of ^{iPr}NHC-functionalized MS and ^{iPr}NHC^{Alk}-functionalized MS were acquired to investigate the topographical characteristics of the NHC film, as shown in Fig. 2C and E, respectively. Island-like structures are observed in ^{iPr}NHC-MS, whereas uniformly distributed globular structures are observed with ^{iPr}NHC^{Alk}-MS. Both these observations are in agreement with the SEM images (Fig. 1B and D). In contrast, imaging of the Ref-MS surface revealed the absence of such structures (Fig. S7 of the SI), confirming that the morphological features observed in both SEM and AFM arise from the NHC films on the electrodeposited surfaces.

AFM-IR was employed to collect IR spectra from nanoscale regions of the electrodeposited surfaces. The AFM-IR spectra obtained on the morphological features (islands and globular) on the ^{iPr}NHC-MS and ^{iPr}NHC^{Alk}-MS show a good agreement with the FT-IR spectra of their respective NHC precursors (Fig. 2A and B). Additionally, the AFM-IR spectra exhibit a prominent peak at 1680 cm^{-1}. As mentioned previously, this could be assigned to byproducts such as urea derivatives which are known to form during NHC deposition.[11,20,30–32,38] Moreover, ^{iPr}NHC^{Alk}-MS exhibits a bit higher thickness with an average of 50–55 nm and high uniformity in distribution as compare to ^{iPr}NHC-MS having average thickness of 30–35 nm (Fig. S8, SI). Further, the laser was tuned to the vibrational frequency of surface molecules, enabling the acquisition of chemical maps that depict the distribution of specific functional groups on the surface. Chemical maps for the ^{iPr}NHC-MS (Fig. 2D) and ^{iPr}NHC^{Alk}-MS (Fig. 2F) were generated by tuning the AFM-IR laser to 1275 ± 1 cm^{-1} (C–N stretching frequency)[34–36] and 1260 ± 1 cm^{-1} (C–H wagging frequency in propargyl group)[37] respectively. As shown in Fig. 2D–F, the AFM-IR maps display amplitude variations at theses frequencies, represented by a color gradient from blue to yellow through red. The yellow regions indicate a higher intensity of the specific moiety, while blue regions signify its absence (background). Comparing the chemical maps (Fig. 2D and F) with the topographical images (Fig. 2C and E) reveals that the morphological patterns on the electrodeposited surfaces correspond to areas with higher vibrational frequency intensity, confirming the localized presence of NHC.

Subsequently, the presence and the composition of carbenes on ^{iPr}NHC-MS and ^{iPr}NHC^{Alk}-MS were assessed by X-ray photoelectron spectroscopy (XPS).[2,15,20,32] The XPS survey spectra (Fig. S9 of the SI) confirm the presence of expected elements C, O, Fe, and N for all samples. Consistent with the deposition of ^{iPr}NHC-MS and ^{iPr}NHC^{Alk}-MS, an increase in N content is detected. The acquired high-resolution N 1s spectra, shown in Fig. 3A and S10, exhibit a distinct peak at 400.2 eV for ^{iPr}NHC-MS and ^{iPr}NHC^{Alk}-MS in contrast to Ref-MS. The peak at 400.2 eV is assigned to the presence of chemically bonded carbene to the MS surfaces, whereas the peak at 399.8 eV could be due to the multilayer nature of carbene adsorption or the

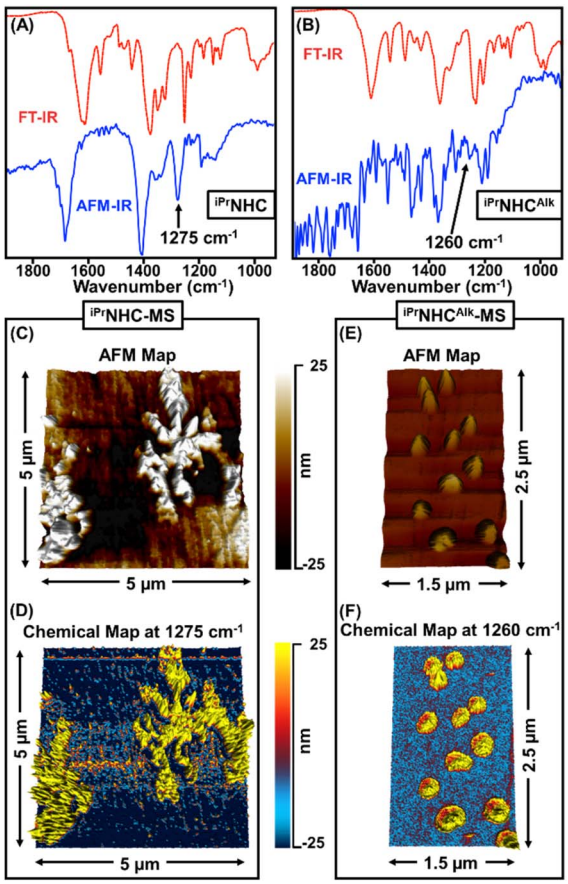

Fig. 2 AFM-IR measurements were collected on both ^{iPr}NHC-MS, and ^{iPr}NHC^{Alk}-MS. Graphs (A) and (B) show the FTIR spectra (red-dashed) of bulk powder, and AFM-IR spectra (blue-line) obtained on NHC-electrodeposited mild steel surface by ^{iPr}NHC·H_2CO_3 and ^{iPr}NHC^{Alk}·H_2CO_3, respectively (C and D) AFM image and chemical maps acquired on ^{iPr}NHC-MS by tuning the IR laser to 1275 cm^{-1}(C–N stretching frequency), and (E and F) AFM image and chemical maps acquired on ^{iPr}NHC^{Alk}-MS by tuning the IR laser to 1260 cm^{-1}(C–H wagging frequency).

presence of any associated by-products of carbene on the NHC-MS surface (Fig. 3A).[5,15]

Given the anticipated crucial role of water and inherently dissolved O_2 in the electrochemical deposition of carbenes (Scheme 1), several control experiments were conducted to assess their impact on NHC deposition on MS. These experiments included electrodeposition in the presence and absence of trace water, under anaerobic conditions by purging with N_2, and using a single-potential deposition at −1.1 V as in literature[13,39] for the same duration as the double-pulse method. The N atomic % from XPS was used to quantify the deposition on the surfaces and is presented in Fig. 3B and C and tabulated in Table S2 (SI). The highest N content was observed (2.8%) on surfaces electrodeposited using the double-pulse method in the presence of trace water, aligning with the proposed mechanism in Scheme 1C. Comparing the N content obtained using the single-pulse method (1.4%) with that of the double-pulse method (2.8%), confirms the enhanced efficiency of deposition achieved through the double-pulse technique.

Interestingly, even in the absence of water, NHC deposition is still observed with 1.3% N content, indicating the involvement of dissolved O_2 in the reaction mechanism. This can be attributed to trace H_2O from atmospheric moisture, dissolved O_2, and the use of a non-anhydrous solvent, all of which contribute to the presence of H_2O and moisture during electrodeposition under ambient conditions. When the electrolyte solution was degassed by purging with N_2, a significant reduction in N content on the deposited surface was observed, comparable to the untreated Ref-MS. These observations establish the successful deposition of NHCs on MS surface *via* electrochemical deposition. Deposition parameters were optimized to enhance NHC coverage on the MS (detailed in SI). Briefly, the highest NHC coverage after optimization (Scheme S11 SI) was achieved by applying a first potential of −0.1 V for 5 ms, followed by a second potential of −1.1 V for 5 s, alternating for 50 cycles using a 5 mM NHC solution with 50 mM H_2O under ambient conditions.

ROS generation and their role in NHCs coating on MS surface

The plausible role of inherently dissolved oxygen in terms of NHC film formation was analyzed in greater detail, given that the applied potential range for carbene deposition spans oxygen reduction reaction (ORR) potential. To this end, CV measurements were performed in a solution composed of 0.1 M NBu_4PF_6 as supporting electrolyte and 5 mM ^{iPr}NHC·H_2CO_3 under both ambient and deaerated conditions. As shown in Fig. 4A and S12, a strong reduction peak at −0.6 V (*vs.* Ag/Ag^+) was observed under ambient conditions, however, this reduction peak becomes less intense when the electrolyte solution was purged with nitrogen gas and hence is ascribed to ORR. This suggests that O_2 is being reduced at the surface during the carbene deposition process and thereby could potentially influence the NHC deposition. A typically well-known ORR mechanism involves 2 + 2 electron transfer, wherein the intermediate is a reactive oxygen species (ROS) formed by the initial two electron transfer to O_2, followed by accepting two more electrons to form the final product ($O_2 \rightarrow O_2^{\bullet-} \rightarrow H_2O_2 \rightarrow H_2O$).[38,40–46] To prove the likely role of ORR during NHC deposition *via* the involvement of these ROS species, various electrochemical measurements were performed exploring both the macro- and the micro-scale. At the macroscale, rotating-disk-electrode (RDE) measurements were conducted, while at the microscale, scanning electrochemical microscopic (SECM) experiments were performed to probe the ORR electron transfer pathway *i.e.*, whether under NHC deposition conditions a 2 + 2 electron transfer occurs involving ROS species.[40,47–49] Initially, RDE measurements were performed using a central gold disk electrode in a solution of 0.1 M NBu_4PF_6 in MeCN, while sweeping the potential at the disk from 0.5 to −1.0 V *vs.* Ag/Ag+. As shown in Fig. S13, a significant ORR current is generated beyond −0.7 V at the disk electrode, which increases with rotation speed (rpm) due to increased mass transport of O_2 at the electrode.[42,50,51] If ORR proceeds *via* the 2 + 2 electron

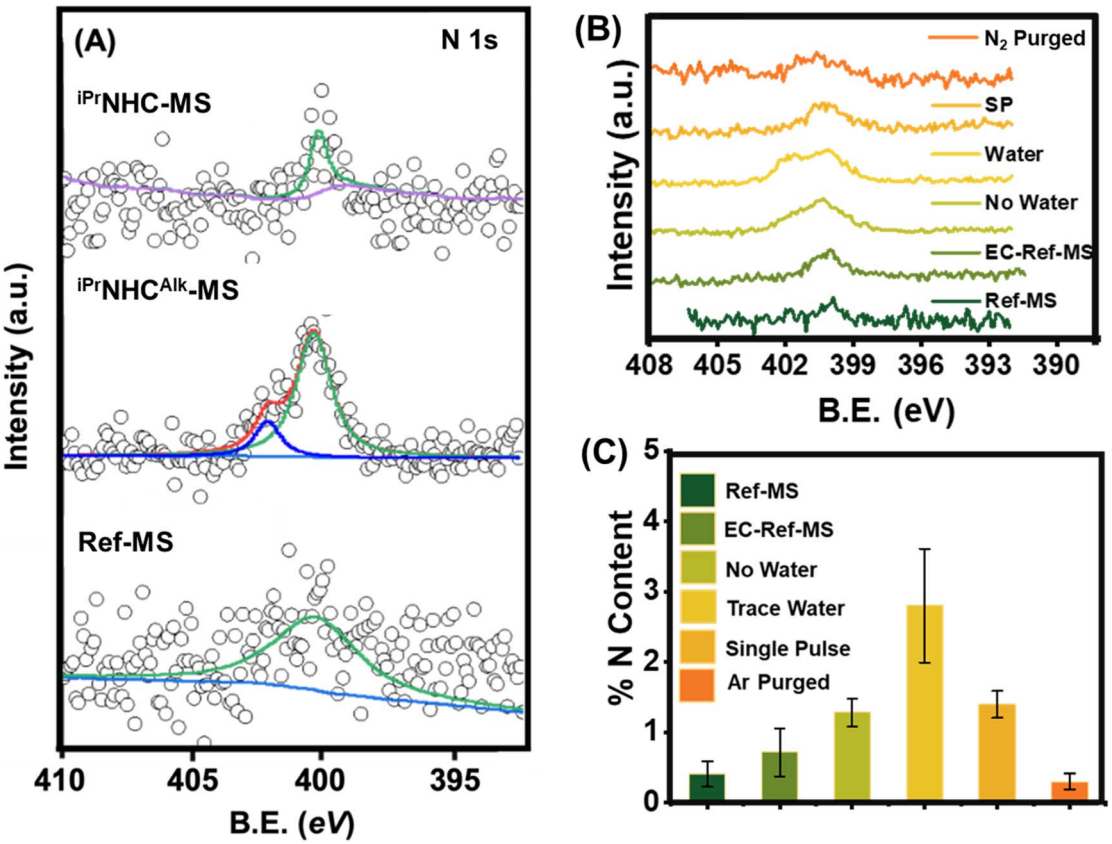

Fig. 3 X-ray photoelectron spectroscopic measurements were conducted on the two NHCs-MS surfaces compared with the bare MS surface. Fitted XPS spectra of (A) N 1s compared for ^{iPr}NHC-MS, ^{iPr}NHC^{Alk}-MS, and Ref-MS surfaces. Role of trace amount of water, dissolved O_2, and double pulse electrodeposition (at −0.5 V and −1.1 V) *versus* single pulse (at −1.1 V) deposition was investigated and represented in (B) comparing respective N 1s spectra, and (C) a bar graph showing the direct comparison of N content (%) derived from (B) for ^{iPr}NHC^{Alk}-MS with data compared to Ref-MS. Error bars represent one standard deviation of three points on the surface.

transfer mechanism, ROS species will form near the electrode surface, which can aid the generation of free carbene by deprotonating the NHC precursor either directly or indirectly. Therefore, to confirm the resultant ORR mechanism, the number of electrons transferred during the reduction process was determined using the Koutecký–Levich (K–L) equation based on the RDE data (more detail in the experimental section).[40,50,51] The K–L plot represents the relationship between the measured current and the square root of the rotation speed, where a linear trend indicates diffusion-controlled kinetics, and the obtained slope can be used to calculate the number of electrons involved in the ORR. As expected a linear relationship was obtained between the measured current and the square root of the rotation speed (Fig. S13). The slope obtained from this K–L plot was then used to calculate the number of electrons transferred during the potential-dependent ORR process. The number of electrons transferred increased from 2.1 at −0.7 V to 4.2 at −1.0 V, suggesting a potential-dependent stepwise reduction of O_2 involving the 2 + 2 electron transfer mechanism. At lower negative potentials (*e.g.*, −0.7 V), O_2 undergoes an initial two-electron reduction to form ROS intermediates, whereas at more negative potentials (*e.g.*, −0.9 V), the reduction proceeds further to produce OH^-/H_2O.[42]

While the RDE results confirm ROS generation, they were conducted on a gold surface rather than the MS surface, wherein the surface plays a key role for the ORR electron transfer mechanism.[43] Therefore, we performed SECM measurements in the sample generation-tip collection (SG-TC) mode to identify the scenario of plausible ROS generation on the MS surface locally. SECM involves a four-electrode setup where the MS surface acts as the substrate (working electrode 1; WE1) and a Pt microelectrode (Ø 25 μm) as the tip (working electrode 2; WE2) which was positioned approximately 10 μm above the substrate (Fig. 4B). To investigate ORR in SECM, the MS substrate was polarized stepwise at increasingly negative potentials to initiate ORR, while the Pt tip was held at a fixed positive potential (+0.8 V *vs.* Ag/Ag^+) to detect any ROS species generated at the substrate–tip interface by oxidizing it back to O_2.[46] This allowed us to monitor the generation and collection of any short-lived ROS species produced locally during the ORR process. As shown in Fig. 4C and D, when the substrate potential was swept from −0.1 V to −0.6 V, the reduction current for ORR at the MS substrate increased significantly (from −67 nA to −129 nA), indicating enhanced ORR as the potential moves more cathodically. Simultaneously, at the Pt-tip, a relatively high oxidation current (around 149 pA) was

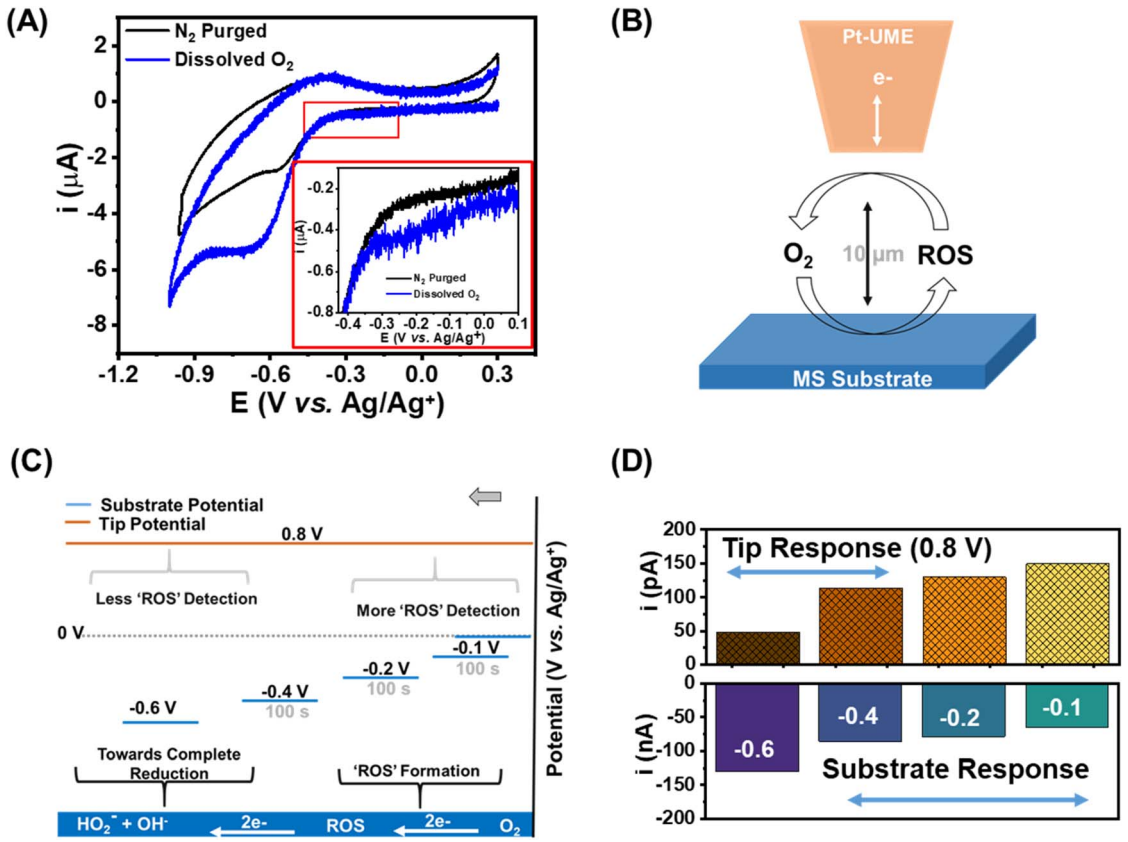

Fig. 4 Mechanistic insights towards the plausible contribution of reactive oxygen species (ROS) on MS surface resulting from the reduction of dissolved oxygen in the MeCN electrolyte conditions composed of 0.1 M NBu_4PF_6. (A) Cyclic voltammetric measurements over MS surface both with and without N_2 purging of the electrolyte solution. Microelectrochemical investigation approach to trace the ROS in close proximity to the MS substrate is schematically shown in (B) representing the applied substrate potential and the UME tip potential in the SG-TC mode of SECM (C) SG-TC scheme for the possible reduction of O_2 to ROS at the substrate and its detection at the tip, and (D) bar graph for the electrochemical response collected at the MS surface at various applied reduction potentials, and concomitant oxidative current response at the UME tip.

detected at less negative substrate potentials (*e.g.*, −0.1 V), confirming that ROS are generated at these lower reduction potentials. However, as the substrate potential became more negative, the oxidative current at the Pt tip gradually decreased (50 pA at −0.6 V) even though the ORR current at the substrate continued to increase (Fig. 4C and D). This inverse relationship between the substrate and tip currents suggests a shift in the reaction pathway. So, at lower overpotentials, oxygen is reduced *via* a two-electron mechanism involving ROS intermediates (such as hydrogen peroxide or superoxide) whereas at higher overpotentials either a direct 4 electron transfer occurs, or a quick 2 + 2 electron transfer occurs with extremely short-lived intermediate(s). As the potential becomes more negative, these intermediates are more likely to undergo further reduction directly at the substrate surface, forming fully reduced products (OH^-/H_2O). These results provide strong evidence for a stepwise ORR pathway (2 + 2 electron transfer) at the MS surface, where intermediate ROS species are initially formed but are eventually consumed as the substrate is driven to more negative potentials.[40,50] These measurements confirm the formation of ROS under employed NHC deposition conditions, which eventually generates more free carbene in close proximity to the MS surface during electrodeposition. Therefore, the electrodeposition of NHC over MS surface under ambient conditions employed is aided by the inherently dissolved oxygen either directly due to ROS species or their indirect ability to form OH^-.[40,44,52]

To gain deeper mechanistic insights into the NHC deposition influenced by the applied potential and hence ROS intermediate(s) or OH^- species, the electrodeposition was carried out by applying −0.1, −0.3 and −0.5 V as the first potential (ROS species effect) while keeping the second potential to −1.1 V (OH^-) and collecting XPS measurements for quantification. As shown in Fig. S14 and summarized in Table S3 (SI), the highest N content was observed in the sample where −0.1 V was applied in the first step, compared to samples with −0.3 V or −0.5 V. These findings align with earlier SECM and RDE measurements, which showed that higher concentrations of ROS are generated at less negative potentials, particularly around −0.1 V. This indicates that ROS are generated locally by the reduction of dissolved O_2, which led to the formation of free carbene in close proximity to the MS surface.

Electrochemical and spectroscopic outcomes confirm that dissolved O_2, plays a crucial role for the generation of ROS.

These ROS species allow the generation of free carbene by abstracting protons from the NHC precursor. These observations are in agreement with the previously reported studies, where authors have detailed the formation of ROS species in a mixture of MeCN and water electrolyte.[40] They found that when ROS species are produced, they can either be stabilized by NBu_4PF_6 (making a complex with NBu_4^+) or could react with a trace amount of water to produce more HO^- species locally (Fig. S15 and S16).[40,44,52] Therefore, based on these observations, three possible routes are possible: (A) direct abstraction of acidic proton by ROS species, as confirmed by performing the measurements in nitrogen purged solution, where the absence of O_2 results in significantly reduced NHC deposition, highlighting the crucial role of ROS in this pathway (Fig. 5A) (B) ROS from ORR catalyzing trace water to OH^- (creating more OH^- flux locally), confirmed by a control experiment without adding trace water, where low NHC deposition was observed; or (C) OH^- production by reduction of water (Fig. 5A). These pathways collectively emphasize the crucial roles of ROS and OH^- species, generated from inherently dissolved O_2 and water, in facilitating the electrochemical generation of free NHCs.

Product identification in NHC-MS samples

Although XPS analysis of the NHC-coated MS surface under different deposition conditions shows variations in nitrogen content, it does not clarify the chemical form in which the NHC is present. To address this, LDI measurements were performed on ^{iPr}NHC-MS samples under various control experiments (mentioned above and in Fig. 3B and C), ranging from EC deposition with trace water, no trace water, purged with N_2 (to remove inherently dissolved oxygen) and single pulse deposition. The mass spectra from these experiments provide a more precise identification of the species and byproducts present on the NHC-coated samples (Fig. 1E–G and S17–S19). The peak at 203 m/z corresponds to ^{iPr}NHC and was observed on all coated samples. However, the side products observed under different control conditions varied depending on the electrochemical deposition parameters. In the presence of trace water and oxygen, a peak at 258.3 m/z was observed. We assign this peak to an ^{iPr}NHC-Fe adduct ($C_{13}H_{21}N_2Fe^+$, m/z = 258), likely formed from direct desorption of NHC bonded to the surface through adatoms.

A previous study has shown that NHCs electrodeposited onto iron oxide surfaces can bind either directly through an Fe–NHC bond or *via* the oxide, as Fe–O–NHC.[20] In alignment with these observations, we detected the presence of several products that could be formed from interaction between the NHC and the native iron oxides or hydroxides of the steel surface, such as ^{iPr}NHC–O–Fe ($C_{13}H_{21}N_2$–O–Fe^+, m/z = 274), urea byproduct (^{iPr}NHC=*O* ($C_{13}H_{21}N_2O^+$, m/z = 219)) and ^{iPr}NHCO_2H (m/z = 234) (Fig. 5B, C and S17–S19).[20] In the absence of trace water, the deprotonation mechanism changes wherein the carbene generation becomes less efficient but still feasible due to the presence of inherently dissolved O_2. In this case, the carbene is generated through the direct electrochemical activation by ROS (described above), resulting in a narrower product distribution

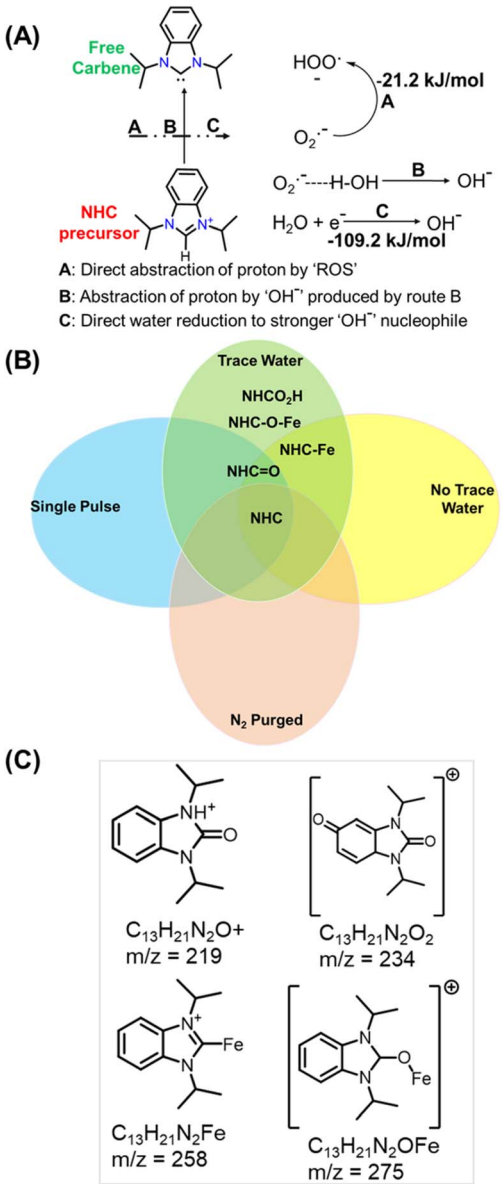

Fig. 5 Proposed reaction pathways and product distributions of ^{iPr}NHC-MS samples prepared under various experimental conditions (A) scheme showing the transformation of an NHC precursor to a free carbene by the involvement of ROS and OH^- along with DFT-predicted free energies for the deprotonation of ^{iPr}NHC·H_2CO_3 by HO^- or ROS species obtained at the B3LYP/def2tzvp level of theory, in SMD (MeCN) (B) Venn diagram summarizing the influence of environmental parameters trace water, pulse electrochemical deposition, and N_2 purging, on observed NHC- and its byproducts (C) plausible molecular structure for NHC-metal and NHC-oxygen species. NHC=O represents the $C_{13}H_{21}N_2O^+$ (m/z = 219); NHC=O–OH represents $C_{13}H_{21}N_2O_2^+$ (m/z = 234); NHC–Fe represents the $C_{13}H_{21}N_2Fe^+$ (m/z = 258) and $C_{13}H_{21}N_2OFe^+$ (m/z = 274) detected in the LDI-MS measurements.

including ^{iPr}NHC–Fe, ^{iPr}NHC=O, and ^{iPr}NHCO_2H. Under N_2 purged conditions, where the inherently dissolved O_2 in the electrolyte was removed, the ^{iPr}NHC-related peaks were almost completely diminished (Fig. 5B, C and S17–S19). This is consistent with the key role of O_2 in promoting carbene

formation that was highlighted in previous experiments. The last scenario of applying only a single cathodic deposition pulse of −1.1 V, being a higher overpotential, tends to limit the extent of ROS generation and eventually limits free carbene formation and surface modification, primarily yielding ^{iPr}NHC and ^{iPr}NHC=O species.[42,44] These observations under different controls highlight how the electrochemical environment, particularly the presence of water and the duration/intensity of applied potential, critically governs free carbene release and its subsequent surface coordination behavior with mild steel.

To complement the microscopic and spectroscopic findings, DFT calculations were conducted to evaluate the energetic favorability of carbene formation from the imidazolium precursor. These simulations were performed at the B3LYP/def2-TZVP level of theory with the SMD implicit solvent model for MeCN (details provided in the SI).[53,54] Fig. 5A and S20–S23 illustrate the potential pathways for abstracting the acidic protons from the imidazolium precursor to generate free carbene. The energy scans indicate that all transitions are barrier less (see SI). Thermal activation *via* hydrogen carbonate, as commonly proposed for immersion-based NHC deposition, was calculated to be endergonic, with a free energy change of +78.0 kJ mol^{-1}. This process yields H_2CO_3, which subsequently dissociates favourably into H_2O and CO_2. In contrast, reactions with hydroxyl (HO-) or superoxide ($O_2^{\bullet -}$) species were determined to be exergonic, with free energy changes of −109.2 kJ mol^{-1} and −21.2 kJ mol^{-1}, respectively. These results support the hypothesis that electrochemically generated ROS can effectively deprotonate the precursor, leading to the formation of carbene, circumventing the need for thermal activation.

Stability analysis

The stability test of the NHC-coated MS was analyzed under strong alkaline conditions (Fig. S24–S27). For a performance comparison, dodecanethiol was electrochemically deposited on mild steel (MS) under conditions similar to those used for depositing NHCs. The thiol-coated samples are denoted as thiol-MS, and successful deposition was confirmed by XPS through the detection of sulfur signals (Fig. S25, SI). To assess the stability of the coatings, both samples were exposed to strong alkaline conditions (0.1 M NaOH) for 1 hour, followed by optical imaging to evaluate degradation. As shown in Fig. S26, SI, the thiol-MS sample underwent severe corrosion, with numerous corrosion islands forming upon NaOH exposure. In contrast, the ^{iPr}NHC-MS sample exhibited no visible corrosion islands under identical conditions. These results indicate that thiol coatings are unstable in alkaline environments, consistent with previous studies by Widrig *et al.*[55] and Bain *et al.*[56] Following this, the freshly coated samples were exposed to ambient conditions for one week to monitor possible degradation or corrosion. Under these conditions, the thiol-MS samples exhibited significant corrosion, with clear island formation observed within this period (Fig. S27, SI). In contrast, the ^{iPr}NHC-MS samples showed no visible signs of corrosion under identical conditions. These results confirm the superior stability of NHC coatings on MS compared to thiol-based coatings, highlighting the potential of NHCs for practical applications.

Conclusions

This study demonstrated the successful surface functionalization of mild steel (MS) surfaces by a simple and reproducible electrochemical approach. The designed double-pulse electrochemical approach under ambient conditions allowed for an interfacial control of carbene generation for MS surface functionalization by specifically controlling the reduction of both dissolved O_2 and water. Rigorous optimization of the double-pulse electrodeposition conditions yielded a −0.1 V first potential applied for 5 ms, followed by a second potential of −1.1 V for 5 s, repeated for 50 cycles to facilitate the deposition of NHC. The resultant NHC films were analyzed in-depth by SEM, XPS, LDI-MS, and AFM-IR to prove the successful functionalization and study its structure-composition correlation aspects. Surface coverage analysis by SEM and AFM-IR revealed a similar distribution pattern, while LDI-MS and AFM-IR facilitated the chemical identification of NHC on the deposited surfaces. Also, two different precursors result in differences in the film thickness and as well as in topography and the overall distribution in the coated sample. Additionally, XPS data quantification provides insights into NHC presence on the surface. The role of inherently dissolved oxygen in the reaction mechanism is investigated through mechanistic studies at both the macroscale using RDE measurements and the microscale *via* SECM. The NHC film demonstrated notable stability under harsh alkaline conditions (0.1 M NaOH, Fig. S24). A simple, straightforward and highly reproducible electrochemical functionalization technique could prove to be a game changer in several industrial applications requiring surface functionalization of mild steel surface, like corrosion-resistant films. This study explains how the change in the backbone group in NHC structure could potentially influence the obtained coatings.

Author contributions

The manuscript was written through the contributions of all authors. All authors have given approval to the final version of the manuscript.

Conflicts of interest

There are no conflicts to declare.

Data availability

Additional data are provided in the Supporting Information and are available upon request.

Supplementary information: materials, experimental methods, synthetic procedures, calculations related to RDE experiment, as well as additional NMR, XPS, LDI-MS, AFM-IR and DFT calculations. See DOI: **https://doi.org/10.1039/d5ta05828g**.

Acknowledgements

The authors acknowledge research funding from the Government of Canada's New Frontiers in Research Fund (NFRF-2020-00573, grant recipient: Cathleen M. Crudden). All authors acknowledge the technical assistance of Mr Nadim Saadeh for LDI-MS and Ms. Patricia Moraille for AFM-IR. Access to computational clusters was kindly provided by the Digital Research Alliance of Canada.

References

1 M. N. Hopkinson, C. Richter, M. Schedler and F. Glorius, *Nature*, 2014, **510**(7506), 485–496.
2 C. M. Crudden, J. H. Horton, I. I. Ebralidze, O. V. Zenkina, A. B. McLean, B. Drevniok, Z. She, H. B. Kraatz, N. J. Mosey, T. Seki, E. C. Keske, J. D. Leake, A. Rousina-Webb and G. Wu, *Nat. Chem.*, 2014, **6**, 409–414.
3 A. V. Zhukhovitskiy, M. J. MacLeod and J. A. Johnson, *Chem. Rev.*, 2015, **115**, 11503–11532.
4 C. A. Smith, M. R. Narouz, P. A. Lummis, I. Singh, A. Nazemi, C. H. Li and C. M. Crudden, *Chem. Rev.*, 2019, **119**, 4986–5056.
5 L. Jiang, B. Zhang, G. Médard, A. P. Seitsonen, F. Haag, F. Allegretti, J. Reichert, B. Kuster, J. V. Barth and A. C. Papageorgiou, *Chem. Sci.*, 2017, **8**, 8301–8308.
6 T. Zhang, S. B. Khomane, I. Singh, C. M. Crudden and P. H. McBreen, *Phys. Chem. Chem. Phys.*, 2024, **26**, 4083–4090.
7 A. Inayeh, R. R. K. Groome, I. Singh, A. J. Veinot, F. C. de Lima, R. H. Miwa, C. M. Crudden and A. B. McLean, *Nat. Commun.*, 2021, **12**, 1–9.
8 R. L. Thimes, A. V. B. Santos, R. Chen, G. Kaur, L. Jensen, D. M. Jenkins and J. P. Camden, *J. Phys. Chem. Lett.*, 2023, **14**, 4219–4224.
9 G. Wang, A. Rühling, S. Amirjalayer, M. Knor, J. B. Ernst, C. Richter, H. J. Gao, A. Timmer, H. Y. Gao, N. L. Doltsinis, F. Glorius and H. Fuchs, *Nat. Chem.*, 2017, **9**, 152–156.
10 C. M. Crudden, J. H. Horton, M. R. Narouz, Z. Li, C. A. Smith, K. Munro, C. J. Baddeley, C. R. Larrea, B. Drevniok, B. Thanabalasingam, A. B. McLean, O. V. Zenkina, I. I. Ebralidze, Z. She, H. B. Kraatz, N. J. Mosey, L. N. Saunders and A. Yagi, *Nat. Commun.*, 2016, **7**, 1–7.
11 C. R. Larrea, C. J. Baddeley, M. R. Narouz, N. J. Mosey, J. H. Horton and C. M. Crudden, *ChemPhysChem*, 2017, **18**, 3536–3539.
12 Y. Zeng, T. Zhang, M. R. Narouz, C. M. Crudden and P. H. McBreen, *Chem. Commun.*, 2018, **54**, 12527–12530.
13 I. Berg, E. Amit, L. Hale, F. D. Toste and E. Gross, *Angew. Chem., Int. Ed.*, 2022, **61**, e202201093.
14 J. J. Navarro, M. Das, S. Tosoni, F. Landwehr, J. P. Bruce, M. Heyde, G. Pacchioni, F. Glorius and B. Roldan Cuenya, *J. Am. Chem. Soc.*, 2022, **144**, 16267–16271.
15 E. Amit, R. Mondal, I. Berg, Z. Nairoukh and E. Gross, *Langmuir*, 2024, **40**, 10374–10383.
16 A. J. Veinot, M. B. E. Griffiths, I. Singh, J. A. Zurakowski, P. A. Lummis, S. T. Barry and C. M. Crudden, *Mater. Adv.*, 2022, **3**, 6446–6450.
17 J. J. Navarro, M. Das, S. Tosoni, F. Landwehr, M. Heyde, G. Pacchioni, F. Glorius and B. Roldan Cuenya, *J. Phys. Chem. C*, 2022, **126**, 17528–17535.
18 E. Amit, L. Dery, S. Dery, S. Kim, A. Roy, Q. Hu, V. Gutkin, H. Eisenberg, T. Stein, D. Mandler, F. Dean Toste and E. Gross, *Nat. Commun.*, 2020, **11**(1), 1–10.
19 W. Zhang and J. Xu, *Mater. Des.*, 2022, **221**, 110994.
20 L. Laundry-Mottiar, T. M. Suduwella, W. G. K. Senanayake, M. J. Turnbull, A. Juneau, E. Kaur, M. D. Aloisio, T. M. G. Selva, J. D. Henderson, H. Y. Nie, M. Biesinger, J. J. Noel, Y. S. Hedberg, C. M. Crudden and J. Mauzeroll, *Chem. Mater.*, 2025, **37**, 76–86.
21 J. Schlegel, *The World of Steel: on the History, Production and Use of a Basic Material*, 2023.
22 M. Iannuzzi and G. S. Frankel, *npj Mater. Degrad.*, 2022, **6**, 1–4.
23 D. de la Fuente, I. Díaz, J. Simancas, B. Chico and M. Morcillo, *Corros. Sci.*, 2011, **53**, 604–617.
24 A. D. Mercer and E. A. Lumbard, *Br. Corrosion J.*, 1995, **30**, 43–55.
25 M. Chigondo and F. Chigondo, *J. Chem.*, 2016, **2016**, 6208937.
26 A. Kadhim, N. Betti, H. A. Al-Bahrani, M. K. S. Al-Ghezi, T. Gaaz, A. H. Kadhum and A. Alamiery, *Int. J. Corros. Scale Inhib.*, 2021, **10**, 861–884.
27 A. Cinitha, P. K. Umesha and N. R. Iyer, *KSCE J. Civ. Eng.*, 2014, **18**, 1735–1744.
28 G. Koch, J. Varney, N. Thompson, O. Moghissi, M. Gould and J. Payer, *Challenges Corrosion*, 2016, 216.
29 A. Vander Zee, L. Laundry-Mottiar, S. Nikpour, S. Matin, J. D. Henderson, U. Eduok, J. F. Hedberg, D. Zagidulin, M. C. Biesinger, J. J. Noël and Y. S. Hedberg, *J. Electrochem. Soc.*, 2023, **170**, 021501.
30 J. T. Lomax, E. Goodwin, M. D. Aloisio, A. J. Veinot, I. Singh, W. T. Shiu, M. Bakiro, J. Bentley, J. F. DeJesus, P. G. Gordon, L. Liu, S. T. Barry, C. M. Crudden and P. J. Ragogna, *Chem. Mater.*, 2024, **36**, 5500–5507.
31 A. J. Veinot, A. Al-Rashed, J. D. Padmos, I. Singh, D. S. Lee, M. R. Narouz, P. A. Lummis, C. J. Baddeley, C. M. Crudden and J. H. Horton, *Chem.–A Eur. J.*, 2020, **26**, 11431–11434.
32 J. Kaur, G. Asadiankouhidehkordi, V. Singh, A. C. Liberati, A. Diraki, S. Bendahmane, M. D. Aloisio, P. Patel, J. Henderson, F. Ben Ettouil, C. M. Crudden, M. Biesinger, A. Levasseur, C. Moreau and J. Mauzeroll, *J. Mater. Chem. A*, 2025, **13**(28), 22745–22754.
33 J. Hou, B. Xu and Q. Lu, *Nat. Commun.*, 2024, **15**(1), 1926.
34 S. Jamil, H. Y. Gondal, A. Ali, A. Hussain, N. Akram, M. Nisar, M. N. Tahir, M. Ashfaq, A. R. Raza, S. Muhammad, Z. M. Cheema, A. Mustafai and M. Y. Sameeh, *R. Soc. Open Sci.*, 2024, **11**(2), 231094.
35 K. Malek, A. Puc, G. Schroeder, V. I. Rybachenko and L. M. Proniewicz, *Chem. Phys.*, 2006, **327**, 439–451.

36 N. V. Pashchevskaya, M. A. Nazarenko, S. N. Bolotin, A. I. Oflidi and V. T. Panyushkin, *Russ. J. Inorg. Chem.*, 2010, **55**, 1425–1432.
37 R. A. Nyquist, Y. S. Lo and J. C. Evans, *Spectrochim. Acta*, 1964, **20**, 619–627.
38 N. L. Dominique, A. Chandran, I. M. Jensen, D. M. Jenkins and J. P. Camden, *Chem.–A Eur. J.*, 2024, **30**(15), e202303681.
39 L. Amar, R. Mondal, O. Blumen, L. Rekanati, I. Berg, S. Harpaz, D. Sharon and E. Gross, *Angew. Chem., Int. Ed.*, 2025, **137**(19), e202422879.
40 C. O. Laoire, S. Mukerjee, K. M. Abraham, E. J. Plichta and M. A. Hendrickson, *J. Phys. Chem. C*, 2010, **114**, 9178–9186.
41 D. T. Sawyer and J. S. Valentine, *Acc. Chem. Res.*, 1981, **14**, 393–400.
42 V. Viswanathan, H. A. Hansen, J. Rossmeisl and J. K. Nørskov, *ACS Catal.*, 2012, **2**, 1654–1660.
43 M. Luo and M. T. M. Koper, *Nat. Catal.*, 2022, **5**, 615–623.
44 C. Costentin, D. H. Evans, M. Robert, J. M. Savéant and P. S. Singh, *J. Am. Chem. Soc.*, 2005, **127**(36), 12490–12491.
45 A. Latus, J. M. Noël, E. Volanschi, C. Lagrost and P. Hapiot, *Langmuir*, 2011, **27**, 11206–11211.
46 Y. Li, C. J. Miller, L. Wu and T. D. Waite, *Environ. Sci. Technol.*, 2022, **56**, 5820–5829.
47 D. Q. Liu, B. Zhang, G. Zhao, J. Chen, H. Pan and W. Sun, *Chin. J. Catal.*, 2023, **47**, 93–120.
48 D. Polcari, P. Dauphin-Ducharme and J. Mauzeroll, *Chem. Rev.*, 2016, **116**, 13234–13278.
49 S. E. Pust, W. Maier and G. Wittstock, *Z. Phys. Chem.*, 2008, **222**, 1463–1517.
50 A. Tiwari, V. Singh, D. Mandal and T. C. Nagaiah, *J. Mater. Chem. A*, 2017, **5**, 20014–20023.
51 A. Tiwari, V. Singh and T. C. Nagaiah, *J. Mater. Chem. A*, 2018, **6**, 2681–2692.
52 Q. Li, C. Batchelor-Mcauley, N. S. Lawrence, R. S. Hartshorne and R. G. Compton, *J. Electroanal. Chem.*, 2013, **688**, 328–335.
53 A. D. Becke, *J. Chem. Phys.*, 1992, **96**, 2155–2160.
54 T. Lecklider, *EE Eval. Eng.*, 2011, **50**, 36–39.
55 C. A. Widrig, C. Chung and M. D. Porter, *J. Electroanal. Chem.*, 1991, **310**, 335–359.
56 C. D. Bain, E. B. Troughton, Y. T. Tao, J. Evall, G. M. Whitesides and R. G. Nuzzo, *J. Am. Chem. Soc.*, 1989, **111**, 321–335.